

Direct-Current Rotary-Tubular Triboelectric Nanogenerators Based on Liquid-Dielectrics Contact for Sustainable Energy Harvesting and Chemical Composition Analysis

Jiyu Wang,^{†,‡,#} Zhiyi Wu,^{‡,#} Lun Pan,^{‡,§,#} Ruijie Gao,^{§,#} Binbin Zhang,[‡] Lijun Yang,[†] Hengyu Guo,[‡] Ruijin Liao,[†] and Zhong Lin Wang^{*,‡,||}

[†]State Key Laboratory of Power Transmission Equipment and System Security and New Technology, Chongqing University, Shapingba, Chongqing 400044, PR China

[‡]School of Material Science and Engineering, Georgia Institute of Technology, Atlanta, Georgia 30332, United States

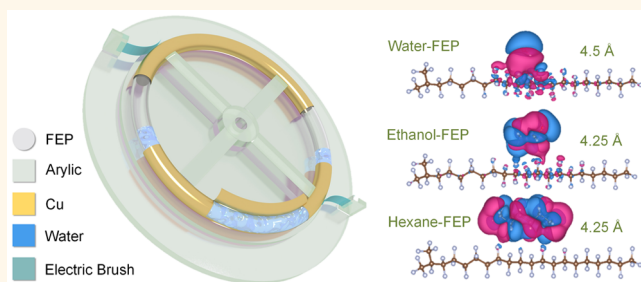
[§]Key Laboratory for Green Chemical Technology of Ministry of Education, School of Chemical Engineering and Technology, Tianjin University, Tianjin 300072, China

^{||}Beijing Institute of Nanoenergy and Nanosystems, Chinese Academy of Sciences, National Center for Nanoscience and Technology (NCNST), Beijing 100083, PR China

Supporting Information

ABSTRACT: Ambient mechanical energy harvesting technology introduces a promising solution to alleviate expanding energy demands on a sustainable basis, of which the drawbacks should attract attention for further advances. In this work, a liquid–dielectrics interface based triboelectric nanogenerator (TENG) with direct-current output is reported as an energy harvester and a chemical sensor, with advantages of feasible fabrication, anti-wearing durability, and low energy consumption. The TENG consisting of an fluorinated ethylene propylene (FEP) tube and Cu electrodes is designed into a ring structure, with two electric brushes bilaterally anchored that converts an alternating-current output into direct-current output. The liquids and copper pellets as the fluid-state dielectrics are prefilled to generate triboelectric charges with an FEP tube. The relevant parameters of TENG are initially optimized, enabling a satisfactory output under rotating excitations. Furthermore, the inherent impacts of various liquids on the output performance of TENG are comprehensively studied, based on which chemical analysis system is developed. Meanwhile, the design for TENG with pellets is also modified for output-current enhancement. Finally, an assembled TENG has been demonstrated not only for energy harvesting without rectification but also for chemical detecting in liquid composition and moisture content analysis. The proposed TENG renders a more-efficient method for energy harvesting and greatly expands its application in direct-current self-powered systems.

KEYWORDS: ambient mechanical energy harvesting, triboelectric nanogenerator, direct-current output, liquid–dielectrics interface, chemical composition analysis



Amidst rising concerns over global warming and the energy crisis, the search for clean and renewable energy sources has been a major challenge facing human society.^{1,2} Generating electricity from ambient energy provides a superior solution to alleviate expanding energy demands on a sustainable basis.^{3,4} Until now, various energy harvesters for scavenging ambient environmental energy have been developed based on electromagnetic,⁵ piezoelectric,^{6–9} and electrostatic¹⁰ transduction mechanisms. However, the widespread

usage of such techniques is likely to be overshadowed by their own drawbacks such as structure complexity,¹¹ single operation frequency,¹² and low energy-conversion efficiency.^{12,13} The emergence of triboelectric nanogenerators (TENGs) to harvest various types of ambient mechanical energy into electricity

Received: December 21, 2018

Accepted: February 5, 2019

Published: February 5, 2019

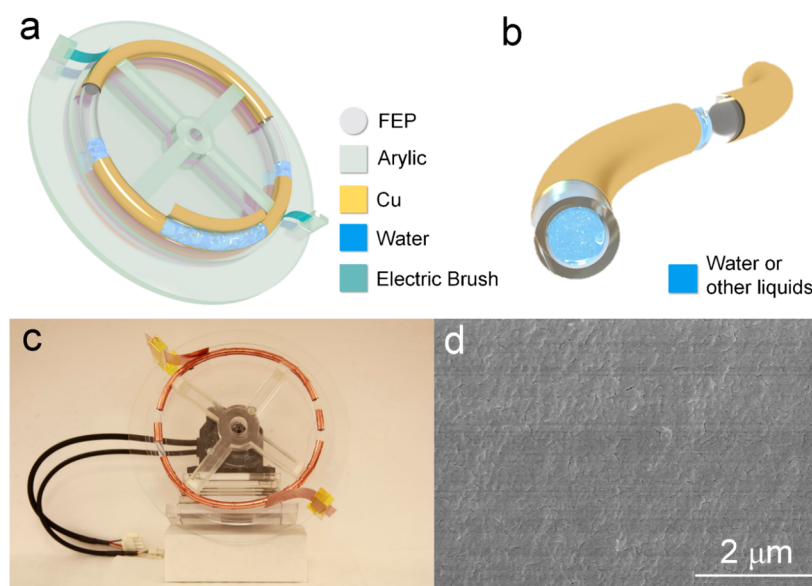


Figure 1. Structural design of the direct-current TENG. (a) Schematic illustration of the ring-tube TENG mounted on a rotating acrylic base with spokes supported, while two electric brushes are installed on an outer stationary acrylic base and clamped by two acrylic blocks. (b) Cross-section view of the extended ring-tube TENG with water or other liquids, in which the liquid is full filled the cross-sectional area. Photographs of (c) as-fabricated TENG on the rotary motor platform. (d) SEM image of the FEP tube (scale bar: 2 μm).

brings about an alternative way for energy conversion and application.^{14–17} Different from the aforementioned energy harvesters, the TENGs, as driven by Maxwell's displacement current, can effectively convert ambient mechanical energy into electricity based on the coupling of triboelectrification and electrostatic induction.¹⁸ Since its creation, the TENG has been demonstrated to harvest a variety of energies that are omnipresent but otherwise wasted in our daily life, such as vibrations,^{19,20} human motions,^{21,22} wind,²³ ocean waves,^{24,25} and so on.²⁶ In addition, the output of TENG can also be used to actively detect the static and dynamic processes arising from mechanical movements for self-powered sensors. With the facile design, flexible structure, and abundant choice of materials, the TENGs have proved to be a simple, cost-effective, and robust technique for self-powered devices and sensors.

Nevertheless, most TENGs normally produce alternating-current electricity due to the alternatively driven induced electrons between electrodes through the periodic physical contact and separation between two dissimilar materials. In this case, a rectification or regulation circuit is required to connect energy storage units for a self-charging power system. Each of these electronic units demands a certain threshold voltage and bring about energy consumption.²⁷ However, the encapsulation of these redundant rectified circuits will enhance the fabrication cost and the difficulties of maintenance. Several research efforts have been devoted to fabricate direct-current TENGs (DC-TENGs) by using the wheel-belt structure²⁸ and the mechanism of air breakdown.²⁹ However, the wheel-belt-based TENG needs a bulky size, and the TENG based on an air breakdown induced ionized air channel cannot regulate the output quantitatively. Thus, a facile and efficient method for realizing DC-TENG needs to be proposed.

Generally, various prototypes of TENGs have been based on friction between solids.³⁰ The performance of solid–solid TENG will be sensitive to environmental factors, resulting in the output instability of TENG,³¹ and the inefficient physical contact area between two abrasive surfaces is another problem

that needs to be settled.³² Alternatively, liquid dielectrics such as water or other fluid dielectrics such as a pile of metal pellets can serve as a favorable substitution to contact with friction layer in TENGs for their relatively stable output and durability.³³ These fluid-state dielectrics with flexible shapes can be easily modulated to fit any designs of TENG, and they can also provide total contact with the solid friction layer to generate more triboelectric charges for a higher output.^{34–36} Furthermore, the flowing property of such dielectrics makes them lubricant for contact, resulting in preferable durability.³² To date, the fluid-state dielectric-based TENGs have not drawn much attention because of irregular and relatively low output. In this regard, a feasible design of the fluid-state dielectric-based TENG with desirable outputs should be formulated, and more importantly, the influence factors on the output performance and the inherent impact of fluid-state properties of this kind of TENG should be systematically studied.

Herein, a multifunctional liquid dielectrics interface based TENG with direct-current output is demonstrated as an energy harvester and a chemical sensor. The TENG that consists of an fluorinated ethylene propylene (FEP) tube and Cu electrodes is designed into a ring tube structure and two electric brushes are bilaterally anchored for producing direct-current electricity on the basis of the freestanding mode for mechanical energy harvesting. The liquids and copper pellets that were employed as the fluid-state dielectrics are prefilled in the tube. As the tube rotates under external stimulus, the fluid-state dielectrics can get total contact with the inner wall of FEP tube, serving a complete cycle of electricity generation. Specifically, the TENG with DI water produces an open-circuit voltage (V_{oc}) up to 228 V and a peak short-circuit current (I_{sc}) of 11.5 μA , while the TENG with copper pellets outputs a V_{oc} up to 101 V and a I_{sc} of 1.27 μA under particular rotating excitations, both of which are direct-current outputs. Furthermore, this kind of TENG can also be applied to analyze chemical composition and concentration. This work provides a more efficient way of

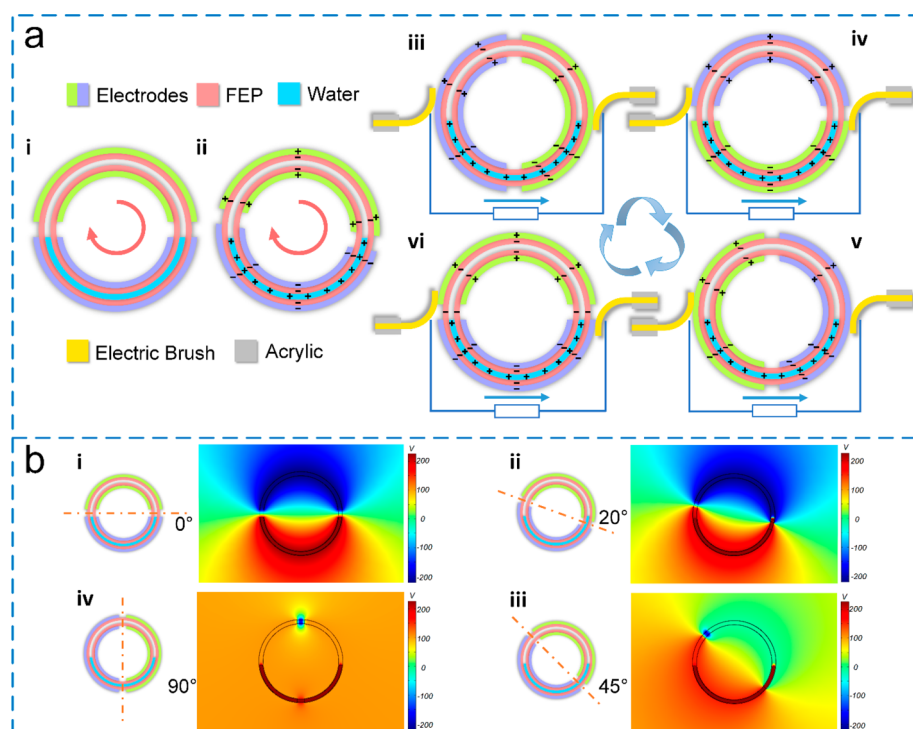


Figure 2. Schematics of working principle of the direct-current TENG. (a) Schematic charge distribution and current direction of the TENG based on a ring structure in both (i, ii) initial status and (iii–vi) stable status. Red arrow shows the rotation direction of the FEP tube. The electricity has generated in one full cycle with the unchanged current direction indicated by the blue arrow. (b) Electric potential distributions on the tube at 4 typical rotation angles from 0° to 90° via COMSOL simulation; the distributions for further rotation angles can be concluded due to the symmetric structure.

energy harvesting and chemical sensing in direct-current self-powered systems.

RESULTS AND DISCUSSION

Structure and Working Mechanism. As illustrated in Figure 1a, the direct-current TENG is designed in a ring tube structure with two electric brushes symmetrically anchored on the both sides of the tube. The tube is mounted on a rotating acrylic base and then fixed by radial supporting spokes that connected with the shaft of the rotary motor. The two electric brushes are installed on an outer stationary acrylic base and clamped by two acrylic blocks, respectively. Once the motor starts to spin, the ring tube will be driven by the rotating base, and the brushes will be bent to get contact with the rotating tube. The tube is made of an FEP tube with transparent and flexible features that serves as the triboelectric material, while the Cu electrodes are covered on the upper and lower semicircular parts of the ring tube. Accordingly, the liquids that employed as the liquid dielectrics are pre-injected in the tube. In virtue of the electronegativity difference between the FEP and such dielectrics, the liquids that flowing in the inner surface of FEP tube will induce the separation of the electrons and the positive charges in the FEP and liquids, respectively. Meanwhile, the charges of Cu electrodes will be induced by the triboelectric charges on FEP, and such induced charges will be moved to the contacted electric brushes. The electric brushes that alternatively contact the Cu electrodes will keep the flow direction of charges unchanged, which is the key strategy to achieve the direct-current output for TENG.

Figure 1b exhibits the cross-section views of ring-tube TENG with water or other liquids. Panels c and d in Figure 1, respectively, show the photographs of the fabricated TENG-

based self-powered system and one single ring-tube TENG, and the scanning electron microscope (SEM) image of the FEP-tube inner surface is exhibited in Figure 1e. Notably, two cut pieces of the Cu films are symmetrically covered on the blank part of tube and are connected with each other through copper wire in measuring voltage to eliminate the effects of floating potential. In addition, the installation positions for electric brushes should be adjusted to be aligned with the fluid-level of dielectric in the tube for maximum signal outputs. The overall TENG system owns the dimensions of 12 in. × 12 in. × 2 in. (more details on the fabrication process are given in the Experimental section).

The working principle of the DC-TENG includes an initial status and a stable status, which are all based on a coupled effect of triboelectrification and electrostatic induction. The detailed electricity generation process of TENG with liquid is illustrated in Figure 2a. At the initial status, the FEP inner tube and the injected liquid should get into full physical contact to create triboelectric charges by rotating a complete circle, with the inner surface of FEP tube being negatively charged and the liquid positively charged according to triboelectric series (i). The negative charges on the inner surface of tube should have an equal amount with the positive charges in the liquid. The stable status begins with the upper electrode starts to enter the liquid covering area, and the lower electrode starts to leave that area (ii), after which the DC-generation process can be divided into four stages. In stage iii, the liquid covering area of the upper electrode increased while that of the lower electrode decreased, and positive charges in the loop will flow from the upper electrode to the lower electrode via the load to screen the local field of the non-mobile negative charges on the FEP tube (iii). The charge transfer continues in the whole process

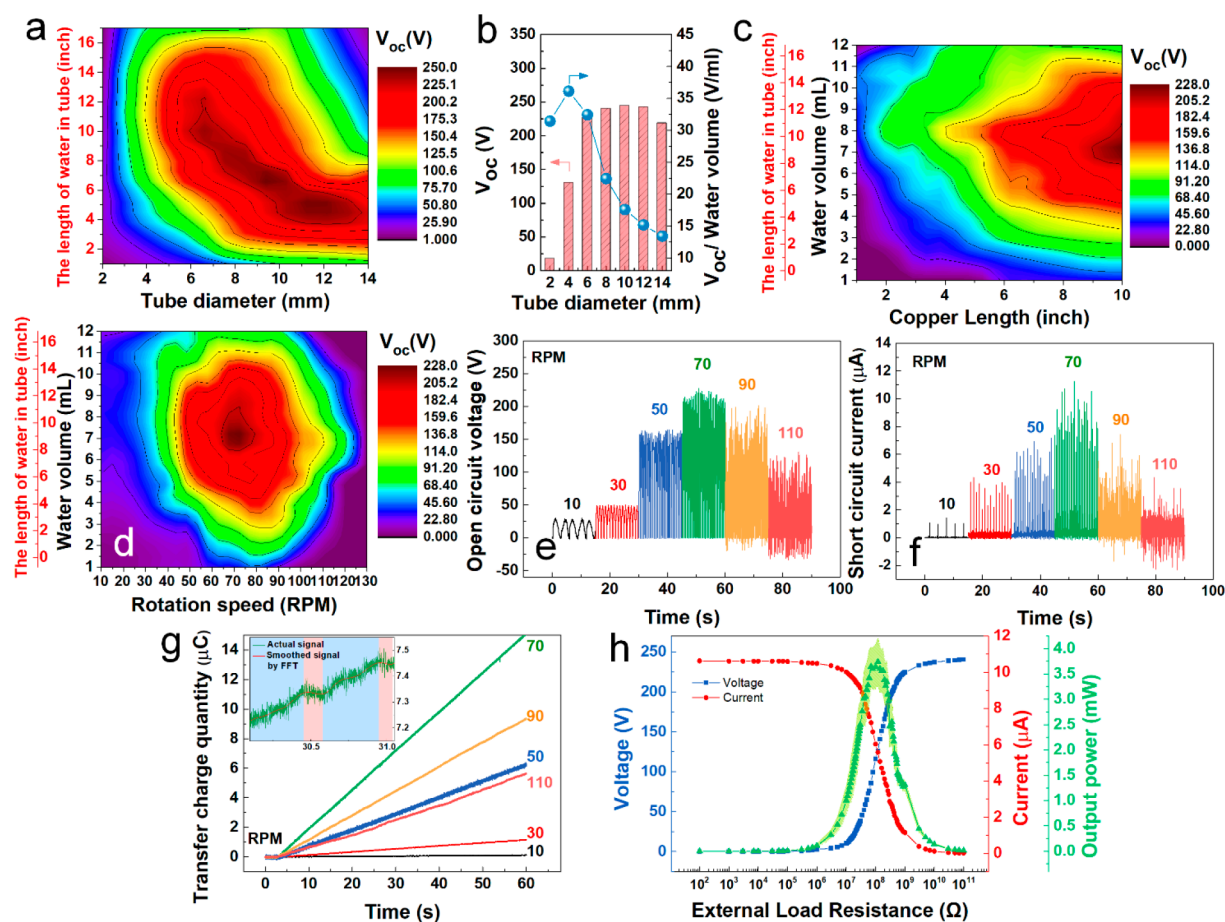


Figure 3. Parameters optimization for TENG fabrication and electrical measurements of TENG with half-filled DI water. (a) V_{oc} of TENGs with different I.D.s of FEP tubes accompanied by a tunable water volume. (b) The maximum peak values of V_{oc} (left column) and V_{oc} per water volume (right column) of TENGs with different I.D.s of FEP tubes under particular water volumes. (c) V_{oc} of TENGs with different copper electrode lengths accompanied by a tunable water volume (left column) and the length of water in the tube normalized by the cross-sectional area of FEP tubes. (d) V_{oc} of TENGs under different rotation speeds accompanied by a tunable water volume (left column) and the length of water in the tube normalized by the cross-sectional area of FEP tubes. (e) V_{oc} (f) I_{sc} and (g) Q_{sc} of TENG under typical rotation speeds of 10, 30, 50, 70, 90, and 110 rpm, respectively. The inset of panel g shows the transfer charge quantity signal with its smoothed signal processed by FFT in one rotating cycle under 70 rpm. (h) Dependences of output voltage, current, and peak powers for TENG under varied resistive loads.

until the upper electrode reaches to the overlap position of the liquid covering area and a new equilibrium is established, which is regarded as the first half cycle of electricity generation (iv). After that, as the tube keeps rotating, the upper electrode intends to rotate back to its original position, and the positive charges will be reversely transferred from the lower electrode to the upper one to rebalance electrostatic status. Unlike other typical AC-TENG structures, the electric brushes directly connected with electrodes are employed for charge transfer. In this case, when the upper electrode starts to leave the liquid covering area, the connected electric brush will thus be switched from to the left one, the direction of charge transfer in the loop will be reversely rectified, resulting in an unchanged current in the load (v). The second half of electricity is, hence, generated as the electrodes rotate back to their original position (vi). In addition, the electricity generation process in the TENG with pellets shares a similar principle with that in the liquid TENG.

For further understanding, the charge distribution in the open circuit condition is also demonstrated, as shown in Figure 2b. Due to the symmetric ring structure of TENG, four particular positions with various rotation angles are selected,

and the continuous variation of the open circuit voltage (V_{oc}) is visualized through finite-element simulation by COMSOL. The V_{oc} is defined as the electric potential difference between two electrodes, which can be produced by the electrostatic induction as the nonmobile negative triboelectric charges on the FEP inner tube are screened in an orderly fashion by the positive ones in the liquid. Therefore, the maximum V_{oc} appears at stage i. When one of the electrodes reaches the overlap position of the liquid covering area, the negative charges on the FEP tube covered by electrode are fully screened by the positive charges in the liquid, resulting in a largest induced potential difference (i). Such a voltage then decreases because two opposite triboelectric charges will be induced on the same electrode as the tube rotates (ii and iii). Once the rotation angle reaches 90° , the V_{oc} comes to the zero-crossing point due to the same amount of the two opposite charges (iv), and the V_{oc} with the same polarity starts to rise until another electrode reaches to the same overlap position. Further rotational movement of the ring tube will induce the V_{oc} proceeds in the same way.

Ring-Tube DC-TENG Optimization (Using DI Water as a Mobile Phase). The output performance of TENG is

primarily concerned with the volume of liquid dielectrics, overlap position, and the operation speed; thus, the related parameters should be initially optimized before fabrication. Correspondingly, as shown in Figure 3a–d, the volume of dielectrics, the tube diameter, the length of the Cu electrode, and the rotation speed were initially explored by comparing the output performances of TENG (indicated by the value of V_{oc}). DI water was employed as the model liquid prefilled in the tube. Figure 3a exhibits the output V_{oc} with varied tube diameters (internal diameter, I.D.) as well as the liquid volume. The liquid volume is normalized by the cross-sectional area of FEP tubes with varied sizes for better comparison. The maximum value of V_{oc} is ca. 228 V, which appears when the I.D. is larger than 6 mm, and the length of water in tube for this maximum value decreases from 10 to 4 in. with a larger I.D. The smaller-diameter TENG exhibits a relatively poor output for a combined effect of the water capacity and fluidity. The tubes with smaller diameters contain less water than the larger ones under the same length of water, and the fluidity will get worse in the narrow cross-section as the water volume increases. Both of them result in insufficient triboelectric charges. Differently, the tubes with larger diameter own better water capacities, and the length of the water therefore decreases to keep the same liquid-covered area with the smaller-diameter tubes as water dispersed in the rotation, leading to a downward trend of the maximum point. Importantly, the energy conversion efficiency is also considered as indicated by the generated V_{oc} per volume of water, with results displayed in Figure 3b. The V_{oc} first exhibits a sharp increase and then remains with a steady trend as the tube diameter raises. The curve of the generated V_{oc} per volume of water, however, has been declining from the I.D. of 4 mm, indicating a lower energy conversion efficiency in the larger-diameter tubes. The I.D. of 6 mm therefore was selected as the optimized diameter value in consideration of the value and the efficiency.

Besides the triboelectrification effect between the liquid and the FEP tube, the final output of the TENG is also generated from the electrostatic induction of the covered Cu electrodes. Hence, the length of the Cu electrodes was optimized according to Figure 3c. It is apparently observed that the output gradually increases with the increase of Cu length and reaches a maximum of ca. 228 V in a Cu length of 10 in., which claims that the induced charge quantity is positively correlated with the length of electrode. As for the raised filled water volume, the output increases initially, followed by a decrease under any fixed Cu length. The smaller water volume cannot provide a sufficient covering area for inducing charges, while a further increase of water volume will cause a reduced area for electrostatic induction on Cu electrode because the extended liquid covering area overlaps the two electrodes simultaneously. With the obtained tube diameter and Cu length, the optimized rotation speed is then discovered (Figure 3d). The maximum output V_{oc} appears under a rotation speed of 70 rpm accompanied by a liquid volume of 7 mL. The rotation speed is closely related with the surface friction of the liquid–solid interface because of the viscosity. The liquid dielectric has viscosity that reflects its resistance to gradual deformation by shear stress. In our case, when the tube starts to rotate, the fluid molecules generally move quicker near the tube wall but slower near the tube's axis, but the viscosity is applied to overcome the relative motion between adjacent molecule layers to keep the fluid static. Once the system reaches

dynamic equilibrium, the surface friction of the liquid–solid interface equals the shear stress of molecules near the tube wall. Based on Newton's law of internal friction, shear stress along with the radius direction can be expressed as the following (detailed calculations are disclosed in the Supporting Information):

$$\tau = -\mu \frac{du}{dr} = -\mu \frac{d}{dr} \left[\frac{\Delta p}{4\mu L} (R^2 - r^2) \right] = \frac{\Delta p}{2L} r \quad (1)$$

where μ is the viscosity coefficient; du/dr is the velocity gradient along the radius direction, which can be further indicated by the pressure drop (Δp) of the tube section at a certain length (L); R is the radius of tube; and r is the current radius value. As the shear stress linearly correlated with the radius value, the surface friction of the liquid–solid interface thus can be expressed as:

$$f = -\tau = -\frac{\Delta p}{2L} R = -\frac{8\mu \bar{u}}{2L} \quad (2)$$

where \bar{u} is the average flow rate, which is positively proportional to the rotation speed. In this regard, when the rotation speed is slower than 70 rpm, the triboelectric charges reduces due to the smaller surface friction, resulting in a decrease of output. In addition, when the water volume is less than 7 mL, the liquid area cannot fully cover the electrode, and the induced charges are thus reduced. While the rotation speed and the water volume are over the extreme points, the length of water in tube will be extended as water further dispersed, and the output hence decreases *via* an excessive overlap of liquid on two adjacent electrodes.

As fabricated by the optimized parameters, the rotary tubular TENG with DI water was then operated on a rotary motor platform with controlled rotation speeds varied from 10 to 130 rpm. The electrical output performances of TENG were tested under different rotation speeds, and the results at typical speeds are shown in Figure 3e–h. As demonstrated in Figure 3e–g, the peak value of V_{oc} first exhibits an upward trend until the rotation speed reaches to 70 rpm, with the maximum peak value of ca. 228 V, which was then followed by a slight decrease. The increase in V_{oc} with the raising rotation speed can be attributed to the increment of triboelectric charges by the enhanced surface friction of the liquid–solid interface as we mentioned above. Once the rotation speed is over than 70 rpm, the water in the tube will be further dispersed causing an extended covering area that overlaps with two adjacent electrodes. Notably, some reversed voltage signals can be observed under a higher rotation speed. This is because some portions of water were driven to the upper part of the tube at some instantaneous speeds, leading to the unchanged induced charges on the same electrode, then the signal will be reversed when this electrode switched to another electric brush. As for the current signal, the I_{sc} mainly includes two parts: the continuous signals produced by the charge transfer between electrodes and the pulse signals generated by the sudden reverse of charge after electrode switch. Both of them are valid signals. The peak value of I_{sc} represents a similar trend as that of output voltage, showing the maximum peak value of ca. 11.5 μA under 70 rpm. The output current can be defined as the transfer rate of triboelectric charges. Therefore, in the ascent stage, the output current will be further enhanced not only by the increment of triboelectric charges but also by the raised transfer rate under a higher rotation speed. While in the

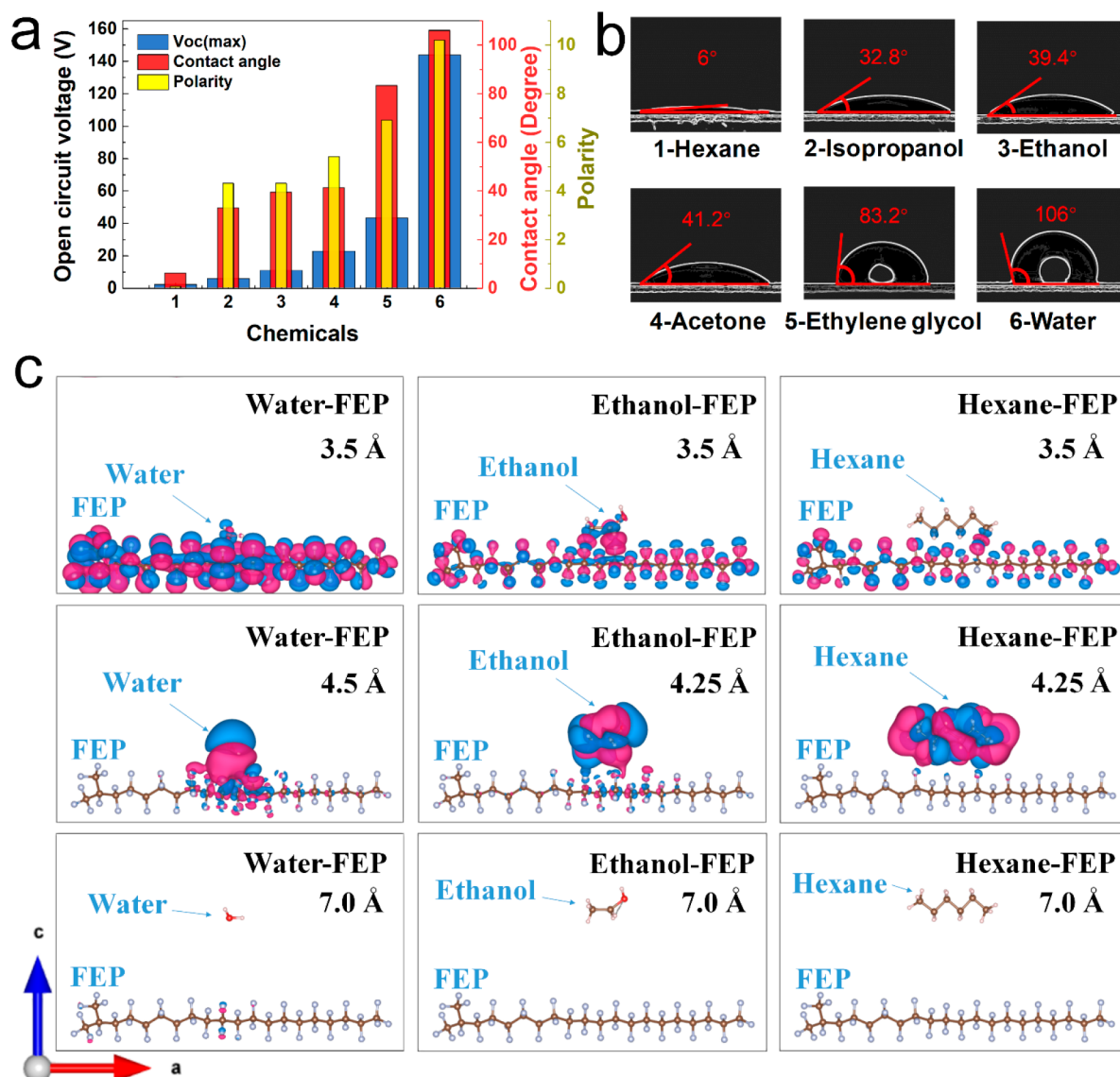


Figure 4. Effects of liquid inherent properties on the output performance of TENG. (a) Relationship between V_{oc} and contact angle and polarity for the discovered liquids (1, hexane; 2, isopropanol; 3, ethanol; 4, acetone; 5, ethylene glycol; and 6, DI water). (b) Contact angle of liquids measured on the FEP substrate. (c) The charge density differences of liquid molecule (water, ethanol, and hexane) and FEP interfaces at different distances (3.5, 4.25–4.5 and 7.0 Å). For water–FEP, ethanol–FEP, and hexane–FEP, the equilibrium distances are calculated to be 4.5, 4.25, and 4.25 Å, respectively.

descent stage, the peak value of I_{sc} experiences further decline, and more reversed current signals are monitored. As the output current is an outcome of both charge quantity and transfer rate, when some portions of water were driven to the upper part of the tube, the charge transfer become will become more disorder even though a slight drop in charge quantity, leading to a significant decrease in the output current.

Meanwhile, the Q_{sc} shows linear charging curves, which are different from that of other TENGs. Because most picoammeters detect the instantaneous charges by measuring the potential variations on their inner capacitors that connected with samples. The potential superposition will be continuous applied on the inner capacitor in the direct-current loop, resulting in a linear growth in the Q_{sc} . The growth rate for the Q_{sc} first increases and then decreases. The maximum value of the Q_{sc} reaches around 14 μC after 60 s of TENG operation under 70 rpm. The inset of Figure 3g shows the enlarged Q_{sc} signal with its smoothed signal processed by fast

Fourier transform (FFT) in one rotating cycle under 70 rpm. In the enlarged view, two main ascent phases are observed followed by short retracing intervals. Due to the symmetric up–down structure, two electrodes will pass through the liquid covering area in one rotating cycle, making the charge quantity increases twice in this cycle. Once one of the electrodes starts to leave the full overlapping position of liquid covering area, the two electrodes will accordingly push apart with their current brushes and become ready to form contact with the opposite ones. During this switching period, there are no charges that transferred between electrodes through the brushes, and the potential of the inner capacitors in picoammeters will thus decay, leading to the detected reduction of charge quantity. In this case, the transfer charge quantity is only detected to be reduced but actually to be stable in the retracing interval because there is no charge dissipation or opposite charge generation. In addition, the charge density ρ_{sc} can also be calculated as 1.32 nC/cm^2 based on the

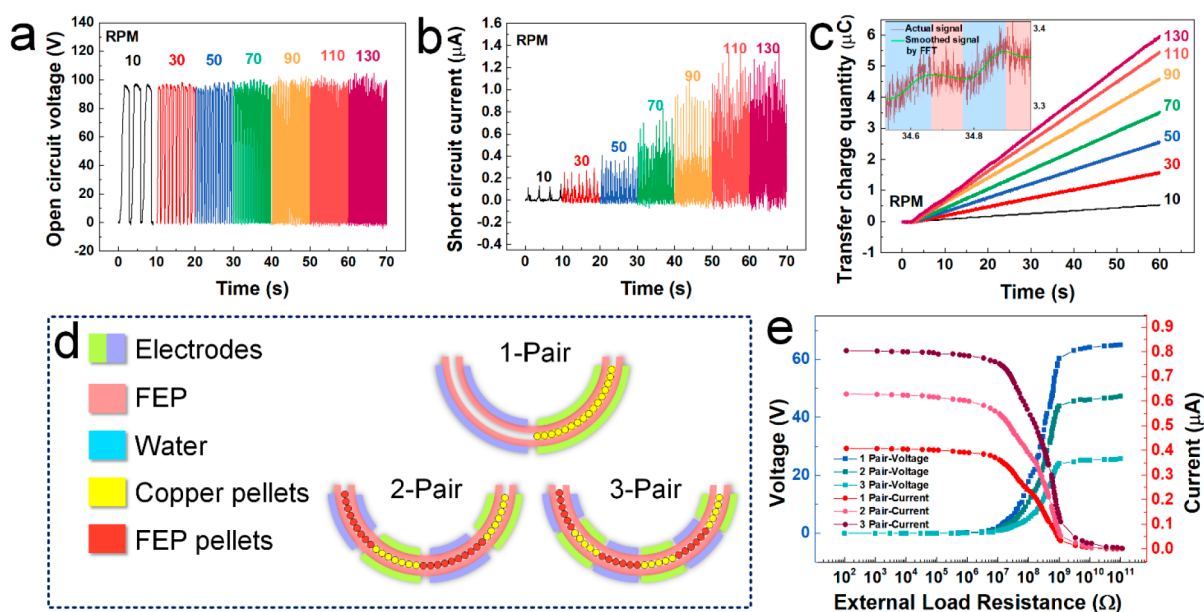


Figure 5. Electrical measurements of TENG with copper pellets. (a) V_{oc} , (b) I_{sc} , and (c) Q_{sc} of TENG with half-filled copper pellets under typical rotation speeds of 10, 30, 50, 70, 90, and 110 rpm, respectively. The inset of panel c shows the transfer charge quantity signal with its smoothed signal processed by FFT in one rotating cycle under 130 rpm. (d) Schematic illustration for the structural designs of TENGs (only displayed the lower semicircular part of the FEP tube) with different pairs of electrodes. Notably, copper pellets and FEP pellets are in different diameters but are sketched as the circles of the same size for better observation. (e) Dependences of output voltage and current for TENG with different electrode pairs under varied resistive loads.

increment of transfer charge quantity in one rotating cycle and the internal surface area of the FEP tube. As displayed in Figure 3h, once an external load is applied, the peak value of I_{sc} decreases as the load resistance increases, while the peak value of V_{oc} follows a reverse trend. The instantaneous output power is maximized at a load resistance of ca. 120 M Ω , corresponding to a peak power density of ca. 3.7 mW under 70 rpm.

Functions of Liquid–FEP Interaction on the TENG Output Performance. To further explore the capability of the rotary tubular TENG, five other kinds of liquids were utilized to investigate the effects of the liquid inherent properties on the TENG output performance. The TENG was operated under the rotary motor platform with a constant rotation speed of 10 rpm. As shown in Figure 4a, the output performances for the liquids of hexane, isopropanol (IPA), and ethanol are relatively low, while the output voltage gradually increases as the liquid varied from acetone and ethylene glycol to DI water. The output voltage of TENG based on freestanding mode is closely related to the triboelectric charges on the solid–liquid interface. Macroscopically, the interface friction is partly contributed by the physical affinity of liquid to FEP tube, which can be reflected by the contact angle. The contact angles of liquids on the FEP substrate were measured and displayed in Figure 4b, exhibiting a positive correlation with the output voltage, while in the micro view, the interface friction is also influenced by the polarity of liquid, resulting from the intermolecular forces.

Regarding to the intermolecular forces, density functional theory (DFT) calculations were therefore performed. A chain-like fluorocarbon containing 21 C atoms and 3 typical liquid molecules (H_2O , ethanol and hexane) were put into a box to consider the corresponding interaction. The kinetic cut-off energy was set to 850 eV, and the k-mesh was set to $1 \times 1 \times 1$. (More-detailed settings are disclosed in the Experimental section). First, the total system energy under different interface

distances is calculated to determine the equilibrium distance at the liquid–FEP interface (Figure S2). All three liquid molecules show the similar variation tendency of the total system energy, which means that the liquid molecule and FEP are in a compressive state when the interface distances are less than the equilibrium value and in a non-contact state when the distance is greater than the equilibrium value. However, their equilibrium values are quite different, in the order of hexane < ethanol < water, which shows a positive correlation with liquid polarity. The charge density differences at the equilibrium distance are calculated to study the contact electrification. As shown in Figure 4c, for the case of water, partial rearrangement of the electrons around the C and F atoms at the interface occurs, and the main charge acceptor of FEP is around the interface F atoms due to the repulsive interaction between water and FEP. For the cases of ethanol and hexane, the charge enrichment around the interface F atoms is also found; however, the degree is in the order of hexane < ethanol < water, positively related to the liquid polarity.

The total charge distribution at different interface distances is further calculated. We chose the interface C and F atoms to show the charge quantity varies with the distance between liquid molecules and FEP. As shown in Figure S3, when the interface distances are less than the equilibrium value, the charge of F becomes larger, and that of H (in liquid molecule) becomes smaller. The variation of charge quantity reaches the maximum value at the minimal distance. That means the compression can result in the accelerative charge rearrangement, which exactly explains why the output performance of TENG exhibits an upward trend with the increasing of the rotation speed. The similar trend also obtained from the cases of ethanol and hexane, and the degree of charge rearrangement is in the order of hexane < ethanol < water, positively related to the liquid polarity.

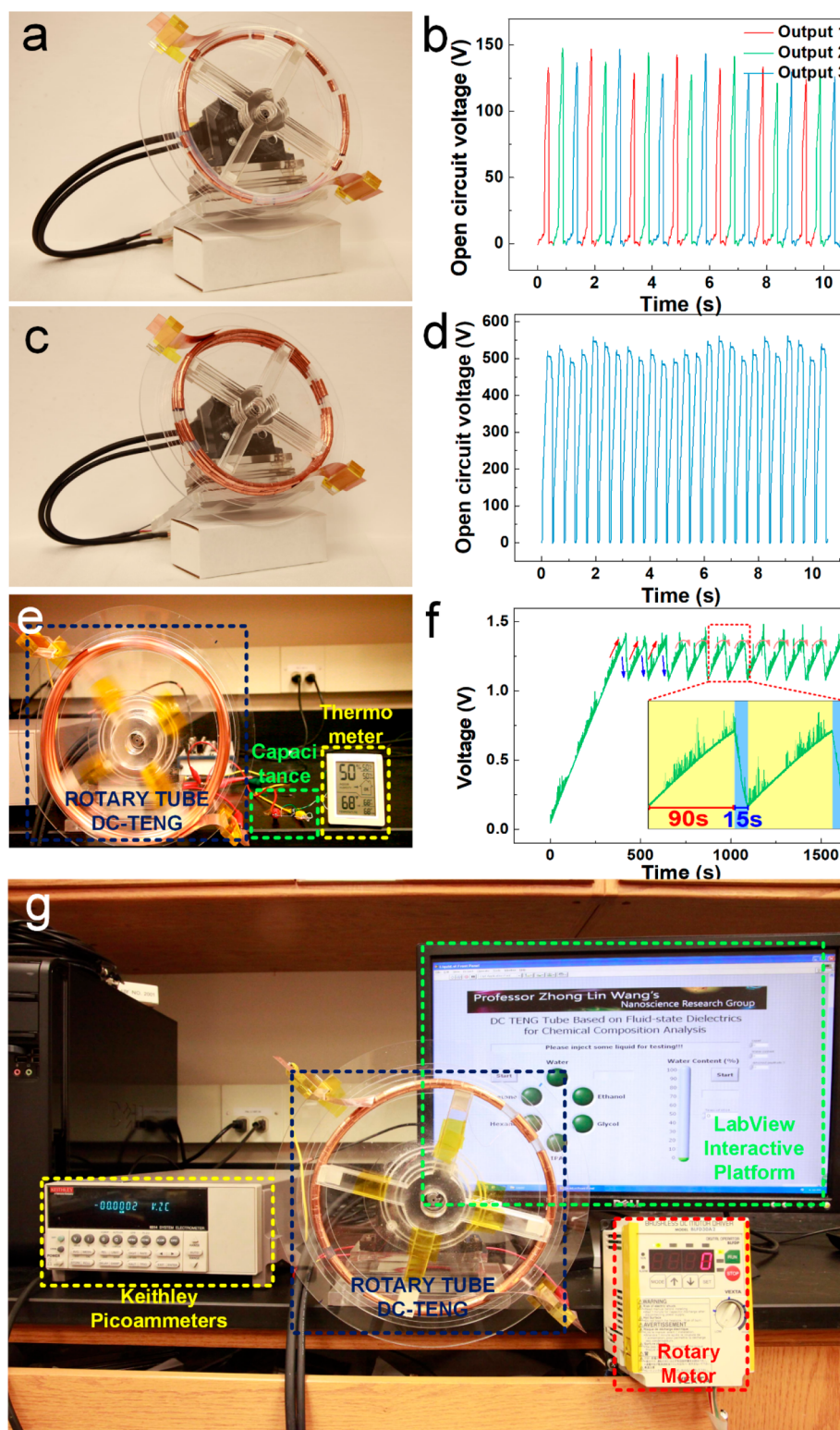


Figure 6. Demonstration of the DC-TENG as a practical power source and a chemical sensor. (a) Photograph of three interlaced assembled TENG with an angular phase difference of 120° between electrodes of adjacent tubes and (b) its output voltage signal. (c) Photograph of the assembled as-fabricated TENGs and (d) its output voltage signal. (e) Photographs of the assembled as-fabricated TENGs as a power source to drive a thermometer through a capacitance without a rectification. (f) Charge–discharge curves of capacitor during energy supply. (g) Photographs of the TENG-based platform used for chemical composition analysis and moisture-content detection.

For the above-mentioned reasons, the output performance of TENG is positively co-affected by the contact angle and polarity of liquid. For instance, ethanol, which has a comparative polarity with IPA, shows a better output

performance because of the higher value of contact angle. However, the output voltage of ethanol is lower than that of acetone as a result of the weaker polarity, although both of them have a similar physical affinity to FEP. More importantly,

such kinds of liquid properties will be altered with the addition of water, leading to the variation of output performance of TENG. With the solution volume unchanged, all of the liquids were mixed with water, and the output signals for liquids with varied concentrations were obtained, with results shown in Figure S4. By virtue of the highly sensitivity to the inner liquids as well as the liquids with varied concentrations, the rotary tubular TENG can be further designed as a sensor to analyze the chemical composition and moisture content of solution, which will be demonstrated in the Demo section (Figure 6g, Movie S2 and Movie S3).

Ring-Tube DC-TENG Optimization (Using Copper Pellets as the Mobile Phase). Aside from the various kinds of liquids, the copper pellets, as another kind of fluid-state dielectrics, can also be utilized in the rotary tubular TENG for energy harvesting. Although the liquids and a pile of pellets both belong to the fluid-state dielectrics, the inherent physical properties are varied and should be properly adjusted into TENG for favorable outputs. Herein, the copper pellets with diameters of 1/16 in. were employed in the same rotary tubular TENG for energy harvesting, with the results under typical rotation speeds shown in Figure 5a–c.

First of all, the peak value of V_{oc} for the copper pellets is lower compared to that for the liquid due to the filled volume deviation. The copper pellets half-filled a tube to avoid blockage in rotation, which makes the triboelectric charges reduced for the less-effective contact area. Then, unlike other liquid dielectrics, the peak value of V_{oc} for copper pellets almost remains stable at different rotation speeds, with a consistent maximum value of ca. 98 V except for a slight decrease in 130 rpm. Moreover, there are no obvious reversed signals observed in V_{oc} for copper pellets. The difference in the voltage signals of two dielectrics is a combined result of viscosity and physical affinity. The liquid dielectric owns the viscosity, with which the surface friction of liquid–solid interface is proportional to the rotation speed, leading to the increase in V_{oc} . If the rotation speed is further raised, the viscosity, however, cannot provide enough shear stress to keep fluid static, the liquid will be dispersed to overlap with two adjacent electrodes, leading to a decline trend. However, the dispersed portion of water will largely affect the induced charge distribution, leading to the reversed voltage signal. The copper pellets are discrete without viscosity so that the surface friction applied on the pellets because the shear stress will convert into rotational kinetic energy, not drive them to move in tube. Besides, only surface friction on the lower surface of the inner wall of tube applied to the pellets system due to the limited filled-pellets quantity. In this way, the pellets system can remain stationary under a relative higher rotation speed but are not likely to move around in the tube to affect the charge distribution, which leads to a constant peak value of V_{oc} without the reversed signal. As the rotation speed further increases to 130 rpm, the surface friction cannot be fully counteracted by the pellets system, and as parts of pellets move freely in the tube, the dynamic balance of pellets system starts to be broken. In this case, the V_{oc} shows a slight decrease of voltage, but only very subtle reversed voltage signals are observed. This is because that the pellets have no physical affinity to the FEP tube, even though some parts of them are driven up to separate the pellet system, and they cannot be attached to the inner wall of tube like liquids. Thus, these sectioned pellets will only affect the charge distribution for a very short time, resulting in very subtle reversed signals.

Conversely, the I_{sc} shows an increase trend with the raising rotation speeds, with a maximum peak value of ca. 1.35 μA at a rotation speed of 130 rpm. Because the transfer charge quantity almost remains constant, the transfer rate of charges is largely enhanced under the increasing rotation speed, producing the increased current. The Q_{sc} exhibits similar linear charging curves with that of liquid-based TENG. The growth rate for the Q_{sc} shows a linearly increasing trend with the raised rotation speed. This is because, with the constant transfer charge quantity, the charging rate is mainly dependent on the output signal frequency, controlled by the rotation speed. Such an increasing rate exhibits a slight drop at 130 rpm, which is a result of reduced charge quantity for the unbalanced pellet system. Additionally, the Q_{sc} signal in one rotating cycle is plotted in the inset of Figure 5c, in which two main ascent phases and retracing intervals are also observed.

By virtue of the discrete characteristic, the copper pellets can be further divided into several separate sections to enhance the output current. The FEP pellets with diameters of 5/32 in. were utilized to totally separate the copper pellets. To maintain the fluidity, the tube was half-filled with pellets, and electrodes were covered on the lower semicircular part of the tube. After the introduction of the FEP pellets, the pairs of electrodes can be raised to form a multielectrode structure of freestanding mode, of which structural designs for 1-pair, 2-pair, and 3-pair arrangements are illustrated in Figure 5d. The copper pellets were divided into several equal parts according to the pairs of electrodes. The length of the electrode was equally split into the same size as the covering area of copper pellets. Because all of the electrodes were mutually connected into groups with two adjacent electrodes in different groups, the covering area of copper pellets can concurrently overlap with only one group, largely enhancing the transfer rate of induced charges. The output voltage and current of TENG with different pairs were obtained at varied external load resistances under a rotation speed of 130 rpm, as plotted in Figure 5e. The voltage overall exhibits a declining trend with the maximum value decreases from 65 V for 1-pair arrangements to 25 V for 3-pair arrangements, which is a result of the reduced induction charges. Although the total transfer charge quantity remains unchanged, the induction charges on each parallel electrode is reduced due to the divided length. However, the current displays a reverse trend with the maximum value of ca. 0.8 μA for 3-pair arrangements. With the unchanged transfer charge quantity, the transfer rate of charge is largely raised by the increasing pairs of electrodes, leading to an increase in the output current. The variations of voltage and current are accorded with the principle of the freestanding mode, in which the decrease of voltage and the increase of current is proportional to the electrode segments.

Applications of the Ring-Tube DC-TENG. The energy output performances of the fabricated TENG were first demonstrated in which three tubular TENGs with various structures were paralleled for different purposes. In Figure 6a, the TENG was coated by the shortened Cu electrode, which covers almost 1/3 of the circumference of the tube. A small cut piece of Cu film was anchored next to the electrode and was used for eliminating the effects of floating potential during voltage single acquisition. After each tube was half-filled with water, the three tubes were interlaced and assembled on the rotary motor, with an angular phase difference of 120° between electrodes of adjacent tubes. The output voltage was obtained under a rotation speed of 60 rpm with the maximum value of

ca. 150 V, as shown in Figure 6b. The output signal is composed of 3 single output signals with a 120° phase difference, which is similar to the typical 3-phase alternating signal after rectification circuit. In addition, the length and the angular phase difference of electrodes can be modified to achieve a multiple-phase signal with adjustable pulse width and shiftable phase difference.

In Figure 6c,d, 3 TENGs with the aforementioned structure were sandwich-like assembled in parallel connection, from which a maximum voltage value of ca. 550 V has been reached. With such a stable output performance, the assembled TENG was demonstrated to drive a thermometer through a capacitor of 100 μF as the energy storage unit, as shown in Figure 6e, and the charge–discharge curves of capacitor are plotted in Figure 6f. The output of TENG can directly charge the capacitor without rectification, and once the voltage of capacitor rose up to about 1.5 V after 90 s of charging time, the thermometer started to work to display the room temperature and humidity (Movie S1). Finally, we've developed a chemical composition analysis system based on the LabView platform. The data for output signals of different liquids and the liquids with varied concentrations were collected and stored as the reference values. The measured liquid was extracted at the specified volume and then injected into the TENG, which was operated on the rotary motor with a fixed rotation speed of 10 rpm. The liquid composition can be analyzed in a fast response after comparing the real-time voltage signal with the reference value. For the given liquid composition, the moisture content of solution can also be analyzed in the same way (Figure 6g, Movie S2, and Movie S3). Furthermore, with more data samples been accumulated, the proposed TENG can be easily and promptly utilized for chemical composition analysis for a variety of liquids with excellent accuracy and reliability, which provides a feasible and effective potential in chemical sensor application.

CONCLUSIONS

In summary, a multifunctional DC-TENG based on liquid dielectrics interface has been demonstrated for energy harvesting and chemical analysis. The TENG consisting of FEP tubes and Cu electrodes is designed into ring structure, in which the liquids and copper pellets as the fluid-state dielectrics are prefilled to serve triboelectric charges, ensuring the favorable anti-wearing durability and stable output regardless of environmental factors. Meanwhile, two electric brushes are bilaterally anchored to alternatively contact the electrodes for delivering direct-current output, by which a rectification circuit and its encapsulation are not required, ensuring the lower energy consumption and economical fabrication cost. Based on the rotary motor platform, the relevant parameters of TENG were initially optimized by investigating the effects of liquid volume, tube diameter, length of electrode, and rotation speed on the output performances of TENG. With the optimized parameters, the electrical output of TENGs with both liquids and pellets were enabled to deliver a satisfactory output under rotating excitations. For the liquid dielectrics, the inherent impacts of various liquids on the output performance were further comprehensively studied based on which the chemical composition analysis system was developed. The chemical analysis system is capable of chemical detecting with an accurate and fast response, which shows potential for liquid detection in TENG-based sensors, while for the pellet dielectrics, a modified design of TENG was also

proposed for enhancing the output current. Finally, an assembled TENG has been demonstrated not only for energy harvesting in powering a thermometer without rectification but also for chemical detection in liquid composition and moisture content analysis. This proposed DC-TENG with fluid-state dielectrics renders a more efficient way toward energy harvesting and greatly expands its application in direct-current self-powered systems.

EXPERIMENTAL SECTION

Fabrication of the TENG. The main body of TENG is fabricated by 1.0 mm thick FEP tube with different inner diameters (I.D. = 2, 4, 6, 8, 10, 12, and 14 mm), which exhibits very high polarity and transparency properties. The FEP tube was first truncated into the specified length (24 in.) and then was curved into a ring structure (I.D. \approx 7.5 in.), with both ends connected through a joint. The joint was a small cut of FEP whose inner diameter equals the outer diameter of the ring tube. After that, two conducting Cu tapes with adhesive back sides (10 in. long, 88.5 μm thick) were symmetrically placed on the upper and lower semicircular parts of the tube. For the needs of the effects investigation, the length of electrode can be tunable to the required length (2, 4, 6, 8, and 10 in.), ensuring the center positions of electrodes unchanged. In addition, 2 short cut pieces of Cu film (1 in. long) were symmetrically placed on the center of the blank part of the tube, which were connected with each other by a copper wire in measuring voltage signal. Finally, 2 pieces of Cu tape with dimensions of 0.4 in. \times 3 in. were placed on both sides of a flexible film (200 μm thick PVC film) with the same size to fabricate the electric brush.

Fabrication of the TENG Platform. The platform is composed of the stationary acrylic base, rotating acrylic plate, and the radial acrylic supporting spokes. For the stationary base, a laser cutter (PLS6.75, Universal Laser Systems) was employed to cut a 1/8 in. thick acrylic sheet into a circular shape (11 in. diameter) with an inner circular hole (1 in. diameter). The rotating plate was also cut from a 1/8 in. thick acrylic sheet into a smaller circular shape (9 in. diameter) with an inner circular hole (0.4 in. diameter). The rotating plate was fixed on the rotary motor with its shaft inserted in the inner circular hole. The supporting spokes were cut from a 1/4 in. thick acrylic sheet into the spoke shape (7.3 in. outer radius, 2 in. inner radius, and 1 in. inner hole radius). The tube was mounted on the rotating base and then supported on radial spokes. In addition, 2 acrylic blocks (2 in. \times 1 in. \times 0.25 in.) with notches were used to clamp the electric brush and then installed on the stationary base.

Characterization and Measurement. A Hitachi SU8010 field-emission SEM was used to measure the inner surface morphology of the FEP tube. A rotary motor (BLFM230-A) was applied to mimic the rotating movements of the tubular TENG, which was controlled by a DC motor driver (Model BLFD30A2). The typical electrical signals of the tubular TENG were acquired *via* an electrometer (Keithley 6514). The software platform was constructed based on LabView, which was capable of realizing real-time data acquisition control and analysis.

Density Functional Theory Calculations. All DFT calculations were carried out with Vienna Ab-initio Simulation Package (VASP).^{37,38} The exchange correlation functional employed was the Perdew–Burke–Ernzerhof functional of generalized gradient approximation.^{39,40} The periodic molecule crystalline model of FEP is consisted of 21 C atoms and used in the calculations. The parameters of FEP were 5.67 \AA \times 5.67 \AA \times 18 \AA . The vacuum region was 20 \AA . The valence electrons were described by a plane wave basis set with the kinetic energy cutoff of 850 eV and the large number of electrons in the outer orbital of the F atom in FEP,⁴¹ and the core electrons were replaced by the projector augmented wave (PAW) pseudopotentials. The k-point was set to 1 \times 1 \times 1, and that of the static method was 1 \times 4 \times 1. The liquid–FEP contact interface distance z is changed in the range from 3.5 to 7 \AA in the calculations, and the denser points from 2 to 3 \AA are to find the equilibrium distance, which is the most-stable state. When the interface distance was

changed, the C atoms in FEP, ethanol, and hexane and the O atoms in water were fixed.

ASSOCIATED CONTENT

Supporting Information

The Supporting Information is available free of charge on the ACS Publications website at DOI: 10.1021/acsnano.8b09642.

Figures showing a schematic diagram of an assumed cylinder, the total system energy under different interface distances, charge quantity variations, and the V_{oc} of TENG; and additional descriptions of the movies in the Supporting Information (PDF)

A movie showing the powering of a thermometer by the DI-water-based TENG without rectification (AVI)

A movie showing a TENG-based platform for chemical composition analysis and water content detecting (part A: chemical composition analysis; part B: water content detecting) (AVI)

A movie showing a TENG-based platform for chemical composition analysis and water content detecting (AVI)

AUTHOR INFORMATION

Corresponding Author

*E-mail: zhong.wang@mse.gatech.edu.

ORCID

Lun Pan: 0000-0002-3083-4693

Ruijie Gao: 0000-0002-6348-284X

Zhong Lin Wang: 0000-0002-5530-0380

Author Contributions

#J.W., Z.W., L.P., and R.G. contributed equally to this work.

Notes

The authors declare no competing financial interest.

ACKNOWLEDGMENTS

Research was supported by the Hightower Chair foundation, the National Key R & D Project from the Ministry of Science and Technology (grant nos. 2016YFA0202704 and 2016YFA0202702), the National Natural Science Foundation of China (grant nos. 51432005, 5151101243, and 51561145021), and the Chinese Scholars Council.

REFERENCES

- Chen, J.; Zhu, G.; Yang, W.; Jing, Q.; Bai, P.; Yang, Y.; Hou, T.; Wang, Z. L. Harmonic-Resonator-Based Triboelectric Nanogenerator as a Sustainable Power Source and a Self-Powered Active Vibration Sensor. *Adv. Mater.* **2013**, *25*, 6094–6099.
- Yang, J.; Chen, J.; Yang, Y.; Zhang, H.; Yang, W.; Bai, P.; Su, Y.; Wang, Z. L. Broadband Vibrational Energy Harvesting Based on a Triboelectric Nanogenerator. *Adv. Energy Mater.* **2014**, *4*, 1301322.
- Wang, Z. L. Triboelectric Nanogenerators as New Energy Technology and Self-Powered Sensors – Principles, Problems and Perspectives. *Faraday Discuss.* **2014**, *176*, 447–458.
- Wang, Z. L.; Chen, J.; Lin, L. Progress in Triboelectric Nanogenerators as a New Energy Technology and Self-Powered Sensors. *Energy Environ. Sci.* **2015**, *8*, 2250–2282.
- Kwon, S.; Park, J.; Law, K. Electromagnetic Energy Harvester with Repulsively Stacked Multilayer Magnets for Low Frequency Vibrations. *Smart Mater. Struct.* **2013**, *22*, 055007.
- Wang, Z. L.; Song, J. Piezoelectric Nanogenerators Based on Zinc Oxide Nanowire Arrays. *Science* **2006**, *312*, 242–246.
- Qin, Y.; Wang, X.; Wang, Z. L. Microfibre-Nanowire Hybrid Structure for Energy Scavenging. *Nature* **2008**, *451*, 809–815.
- Yuan, L.; Lu, X.; Xiao, X.; Zhai, T.; Dai, J.; Zhang, F.; Hu, B.; Wang, X.; Gong, L.; Chen, J.; Hu, C.; Tong, Y.; Zhou, J.; Wang, Z. L. Flexible Solid-State Supercapacitors Based on Carbon Nanoparticles/MnO₂ Nanorods Hybrid Structure. *ACS Nano* **2012**, *6*, 656–661.
- Yuan, L.; Dai, J.; Fan, X.; Song, T.; Tao, Y.; Wang, K.; Xu, Z.; Zhang, J.; Bai, X.; Lu, P.; Chen, J.; Zhou, J.; Wang, Z. L. Self-Cleaning Flexible Infrared Nanosensor Based on Carbon Nanoparticles. *ACS Nano* **2011**, *5*, 4007–4013.
- Okamoto, H.; Hamate, Y.; Xu, L.; Kuwano, H. Optimal Geometry of a Parallelized Electret-Based Vibration Energy Harvester. *Smart Mater. Struct.* **2012**, *21*, 065001.
- Beeby, S.; Tudor, M.; White, N. Energy Harvesting Vibration Sources for Microsystems Applications. *Meas. Sci. Technol.* **2006**, *17*, R175–R195.
- Wang, Z. L. Self-Powered Nanotech-Nanosize Machines Need Still Tinier Power Plants. *Sci. Am.* **2008**, *298*, 82–87.
- Rome, L.; Flynn, L.; Goldman, E.; Yoo, T. Generating Electricity While Walking with Loads. *Science* **2005**, *309*, 1725–1728.
- Wang, Z. L.; Jiang, T.; Xu, L. Toward the Blue Energy Dream by Triboelectric Nanogenerator Networks. *Nano Energy* **2017**, *39*, 9–23.
- Wang, Z. L. Catch Wave Power in Floating Nets. *Nature* **2017**, *542*, 159.
- Fan, F.; Tian, Z.; Wang, Z. L. Flexible Triboelectric Generator! *Nano Energy* **2012**, *1*, 328–334.
- Wang, Z. L. Nanogenerators, Self-Powered Systems, Blue Energy, Piezotronics and Piezo-Phototronics – A Recall on the Original Thoughts for Coining These Fields. *Nano Energy* **2018**, *54*, 477–483.
- Wang, Z. L. On Maxwell's Displacement Current for Energy and Sensors: The Origin of Nanogenerators. *Mater. Today* **2017**, *20*, 74–82.
- Yang, W.; Chen, J.; Jing, Q.; Yang, J.; Wen, X.; Su, Y.; Zhu, G.; Bai, P.; Wang, Z. L. 3D Stack Integrated Triboelectric Nanogenerator for Harvesting Vibration Energy. *Adv. Funct. Mater.* **2014**, *24*, 4090–4096.
- Wang, X.; Niu, S.; Yi, F.; Yin, Y.; Hao, C.; Dai, K.; Zhang, Y.; You, Z.; Wang, Z. L. Harvesting Ambient Vibration Energy over a Wide Frequency Range for Self-Powered Electronics. *ACS Nano* **2017**, *11*, 1728–1735.
- Hua, Q.; Sun, J.; Liu, H.; Bao, R.; Yu, R.; Zhai, J.; Pan, C.; Wang, Z. L. Skin-Inspired Highly Stretchable and Conformable Matrix Networks for Multifunctional Sensing. *Nat. Commun.* **2018**, *9*, 244.
- Zhang, H.; Yang, Y.; Hou, T.; Su, Y.; Hu, C.; Wang, Z. L. Triboelectric Nanogenerator Built Inside Clothes for Self-Powered Glucose Biosensors. *Nano Energy* **2013**, *2*, 1019–1024.
- Wang, J.; Ding, W.; Pan, L.; Wu, C.; Yu, H.; Yang, L.; Liao, R.; Wang, Z. L. Self-Powered Wind Sensor System for Detecting Wind Speed and Direction Based on a Triboelectric Nanogenerator. *ACS Nano* **2018**, *12*, 3954–3963.
- Xi, Y.; Wang, J.; Zi, Y.; Li, X.; Han, C.; Cao, X.; Hu, C.; Wang, Z. L. High Efficient Harvesting of Underwater Ultrasonic Wave Energy by Triboelectric Nanogenerator. *Nano Energy* **2017**, *38*, 101–108.
- Xu, L.; Pang, Y.; Zhang, C.; Jiang, T.; Chen, X.; Luo, J.; Tang, W.; Cao, X.; Wang, Z. L. Integrated Triboelectric Nanogenerator Array Based on Air-Driven Membrane Structures for Water Wave Energy Harvesting. *Nano Energy* **2017**, *31*, 351–358.
- Wang, P.; Pan, L.; Wang, J.; Xu, M.; Dai, G.; Zou, H.; Dong, K.; Wang, Z. L. An Ultra-Low-Friction Triboelectric-Electromagnetic Hybrid Nanogenerator for Rotation Energy Harvesting and Self-Powered Wind Speed Sensor. *ACS Nano* **2018**, *12*, 9433–9440.
- Zi, Y.; Guo, H.; Wen, Z.; Yeh, M.; Hu, C.; Wang, Z. L. Harvesting Low-Frequency (< 5 Hz) Irregular Mechanical Energy: A Possible Killer Application of Triboelectric Nanogenerator. *ACS Nano* **2016**, *10*, 4797–4805.
- Yang, Y.; Zhang, H.; Wang, Z. L. Direct-Current Triboelectric Generator. *Adv. Funct. Mater.* **2014**, *24*, 3745–3750.

- (29) Luo, J.; Xu, L.; Tang, W.; Jiang, T.; Fan, F.; Pang, Y.; Chen, L.; Zhang, Y.; Wang, Z. L. Direct-Current Triboelectric Nanogenerator Realized by Air Breakdown Induced Ionized Air Channel. *Adv. Energy Mater.* **2018**, *8*, 1800889.
- (30) Chen, J.; Wang, Z. L. Reviving Vibration Energy Harvesting and Self-Powered Sensing by a Triboelectric Nanogenerator. *Joule* **2017**, *1*, 480–521.
- (31) Nguyen, V.; Zhu, R.; Yang, R. Environmental Effects on Nanogenerators. *Nano Energy* **2015**, *14*, 49–61.
- (32) Zhang, X.; Zheng, Y.; Wang, D.; Zhou, F. Solid-Liquid Triboelectrification in Smart U-Tube for Multifunctional Sensors. *Nano Energy* **2017**, *40*, 95–106.
- (33) Pan, L.; Wang, J.; Wang, P.; Gao, R.; Wang, Y.; Zhang, X.; Zou, J.; Wang, Z. L. Liquid-FEP-Based U-Tube Triboelectric Nanogenerator for Harvesting Water-Wave Energy. *Nano Res.* **2018**, *11*, 4062–4073.
- (34) Lin, Z.; Cheng, G.; Lin, L.; Lee, S.; Wang, Z. L. Water-Solid Surface Contact Electrification and its Use for Harvesting Liquid-Wave Energy. *Angew. Chem.* **2013**, *125*, 12777–12781.
- (35) Lin, Z.; Cheng, G.; Lee, S.; Pradel, K.; Wang, Z. L. Harvesting Water Drop Energy by a Sequential Contact-Electrification and Electrostatic-Induction Process. *Adv. Mater.* **2014**, *26*, 4690–4696.
- (36) Tang, W.; Jiang, T.; Fan, F.; Yu, A.; Zhang, C.; Cao, X.; Wang, Z. L. Liquid-Metal Electrode for High-Performance Triboelectric Nanogenerator at an Instantaneous Energy Conversion Efficiency of 70.6%. *Adv. Funct. Mater.* **2015**, *25*, 3718–3725.
- (37) Kresse, G.; Furthmüller, J. Efficiency of *Ab-Initio* Total Energy Calculations for Metals and Semiconductors Using a Plane-Wave Basis Set. *Comput. Mater. Sci.* **1996**, *6*, 15–50.
- (38) Kresse, G. *Ab-Initio* Molecular-Dynamics for Liquid-Metals. *J. Non-Cryst. Solids* **1995**, *193*, 222–229.
- (39) Perdew, J.; Burke, K.; Ernzerhof, M. Generalized Gradient Approximation Made Simple. *Phys. Rev. Lett.* **1996**, *77*, 3865–3868.
- (40) Perdew, J.; Wang, Y. Accurate and Simple Analytic Representation of the Electron-Gas Correlation-Energy. *Phys. Rev. B: Condens. Matter Mater. Phys.* **1992**, *45*, 13244–13249.
- (41) Wu, J.; Wang, X.; Li, H.; Wang, F.; Yang, W.; Hu, Y. Insights Into the Mechanism of Metal-Polymer Contact Electrification for Triboelectric Nanogenerator *via* First-Principles Investigations. *Nano Energy* **2018**, *48*, 607–616.